Refractive index sensitivity characteristics near the dispersion turning point of the multimode microfiber based in-line Mach-Zehnder interferometer

HAIPENG LUO,[1] QIZHEN SUN,[1,2*] XIAOLEI LI, [1] ZHIJUN YAN,[2] YANPENG LI,[1] DEMING LIU,[1] LIN ZHANG[2]

[1]*School of Optical and Electronic Information, and National Engineering Laboratory for Next Generation Internet Access System, Huazhong University of Science and Technology, Wuhan 430074, China*
[2]*Aston Institute of Photonic Technologies, Aston University, Birmingham, B4 7ET, UK*
**Corresponding author: qzsun@mail.hust.edu.cn; q.sun2@aston.ac.uk*

Received XX Month XXXX; revised XX Month, XXXX; accepted XX Month XXXX; posted XX Month XXXX (Doc. ID XXXXX); published XX Month XXXX

The turning point of the refractive index (RI) sensitivity based on the multimode microfiber (MMMF) in-line Mach-Zehnder Interferometer (MZI) is firstly observed. By tracking the resonant wavelength shift of the MZI generated between HE_{11} and HE_{12} modes in the MMMF, the surrounding RI (SRI) could be detected. Theoretical analysis demonstrates that the RI sensitivity will be reached to ±∞ on either side of the turning point due that the group effective RI difference (G) approaches to zero. Significantly, the positive sensitivity exists in a much wide fiber diameter range while the negative sensitivity can be achieved in a narrow diameter range of only 0.3μm. Meanwhile, the experimental sensitivities and variation trend at different diameters exhibit high consistency with the theoretical results. High RI sensitivity of 10777.8nm/RIU at the fiber diameter of 4.6μm and the RI around 1.3334 is realized. The discovery of the sensitivity turning points has great significance on trace detection due to the possibility of ultra-high RI sensitivity. © 2015 Optical Society of America

OCIS codes: *(060.2370) Fiber optics sensors; (280.4788) Optical sensing and sensors; (060.2310) Fiber optics; (230.3990) Micro-optical devices.*

http://dx.doi.org/ XXXX /OL. XX. XXXX XX

Fiber-based sensors have been widely investigated for the measurement of chemical and biomedical parameters due to their unique merits, such as compact size, electromagnetic interference immunity, potential low cost, and usage in harsh environment [1–5]. Especially, ultra-high sensitive refractive index (RI) fiber sensors are significant for biochemical trace detection. When the fiber is surface immobilized with functional materials, it can realize selective and accurate biochemical identification [6-8].

Recently, the microfiber, with promising optical properties of large evanescent field, low transmission loss, high nonlinear effect, and tight optical confinement, has become attractive in photonics fields [9–13]. Various researches based on microfiber have been introduced, including resonators [14], lasers [15], supercontinuum generators [16], slow- or fast-light systems [17], and sensors [18]. Significantly, microfiber based sensors always serve as promising candidates for various biochemistry applications due to their high RI sensitivity beneficial from the large evanescent field.

One kind of microfiber i.e. multimode microfiber (MMMF), also called non-adiabatic tapered fiber, is simply fabricated through tapering a conventional single mode fiber (SMF) into micrometer size. Different from the adiabatic tapered fiber, the MMMF has a much larger transition angle [19], resulting in the excitation of few guided modes inthe transition region. Then, an in-line Mach-Zehnder interference (MZI) is generated in only one standard microfiber due to the interference between the two dominant modes. MMMF has shown outstanding performance in refractive index (RI) sensing with high sensitivity of 10^3～10^4nm/RIU [20-22] and temperature sensing with the sensitivity up to -3.88nm/°C [22]. However, to the best of our knowledge, systematic investigation on the sensing performance of the MMMF based in-line Mach-Zehnder interferometer (MZI) especially the RI sensitivity characteristics has not been reported.

In this letter, we establish the RI sensing modal and systematically analyze the sensitivity of the MMMF based in-line MZI. By comprehensively calculating the effective RI of the supporting modes, the mode field distribution, and the group effective RI difference, the RI sensitivity of the sensor can be obtained. The simulation results reveal that the RI sensitivity will be significantly enhanced and reached to ±∞ when the group effective RI difference approaches to zero, which is defined as the dispersion turning point. Moreover, RI sensing experiments of microfibers with different diameters are carried out to demonstrate the variation trend of the sensitivity and the validity of the theory. Specifically, the RI sensitivity higher than 10^4nm/RIU is achieved.

Fig. 1 exhibits the schematic diagram of the MMMF based fiber sensor structure, which consists of the Lead-in SMF (LISMF), the first taper region, a section of MMMF, the second taper region, and the Lead-out SMF (LOSMF). The sensor is simply fabricated by bilateral tapering the SMF to several micrometers with the help of hydrogen flame. When light transmits from the LISMF into the MMMF, the

fundamental mode and the first high order mode i.e. HE_{11} mode and HE_{12} mode are excited simultaneously due to the non-adiabatic taper structure [23]. Then, the two modes are collected through the second taper region and then transmitted out through the LOSMF. As an optical path difference existing between the HE_{11} and HE_{12} modes, a periodic interference spectrum of the in-line MZI is generated in the single fiber.

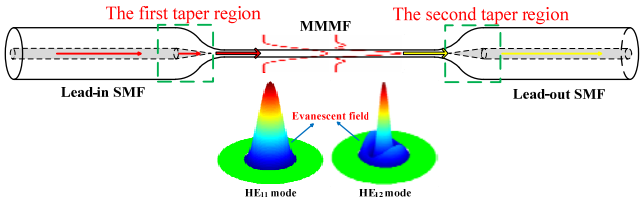

Fig. 1. Schematic diagram of the sensor, the inset presents typical 3D electrical field distribution of HE_{11} and HE_{12} modes in MMMF with the diameter of 8μm.

The resonant dip λ_m generated by the in-line MZI between the HE_{11} mode and the HE_{12} mode can be expressed as:

$$\begin{aligned}(n_1 - n_2)L = \Delta n_{eff} L = \left(p + \tfrac{1}{2}\right)\lambda_m \\ \Delta n_{eff} = n_1 - n_2 = (\beta_1 - \beta_2) \times \frac{\lambda_m}{2\pi}\end{aligned} \quad (1)$$

where n_1 and n_2 , β_1 and β_2 are the effective RI and propagation constants of the HE_{11} mode and the HE_{12} mode, respectively. Δn_{eff} is the effective RI difference between the two modes, L represents the length of MMMF, and m is a positive integer.

For a tapered SMF, with the waist diameter of several micrometers, the core diameter of the waist is under sub-micrometer to be neglected, and thus, the tapered SMF are considered to be a uniform medium with the same material of the SMF cladding. β_1 and β_2 in MMMF can be calculated from the waveguide field equations as follows [24]:

$$\begin{aligned}&\left\{\frac{J_1'(U)}{UJ_1(U)} + \frac{K_1'(W)}{WK_1(W)}\right\} \times \left\{\frac{J_1'(U)}{UJ_1(U)} + \frac{n_{SRI}^2}{n_0^2}\frac{K_1'(W)}{WK_1(W)}\right\} \\ &= \left\{\frac{\beta}{k_0 n_0}\right\}^2 \left\{\frac{V}{UW}\right\}^4 \\ &U = \frac{D}{2}\left(k_0^2 n_0^2 - \beta^2\right)^{1/2} \\ &W = \frac{D}{2}\left(\beta^2 - k_0^2 n_{SRI}^2\right)^{1/2} \\ &V = k_0 \times \frac{D}{2}\left(n_0^2 - n_{SRI}^2\right)^{1/2}\end{aligned} \quad (2)$$

where J_1 is the first order form of the first kind Bessel function, and K_1 is the first order form of the second kind modified Bessel function, n_{SRI} and n_0 are the RI of surrounding medium and MMMF, respectively, β is the propagation constant of HE_{1m} mode, D is the diameter of MMMF, and k_0 is the propagation constant in vacuum.

Fig. 2 presents the calculated effective RI i.e. n_{eff} and the proportion of evanescent field (η) of HE_{11} and HE_{12} modes in SRI of 1.3320 as a function of diameter based on Eq. (2). As we can see, n_{eff} increases while η decreases along with diameter increase, owing that larger proportion of light will be confined in MMMF when the diameter increases. Besides, each mode has a cut-off diameter, which is defined as the fiber diameter corresponding to the mode cut-off. For example, the value of HE_{11} mode is 0.54μm, as well as that of HE_{12} mode is 3.68μm. When the diameter of MMMF is below the cut-off diameter, such a mode will not be supported in the MMMF.

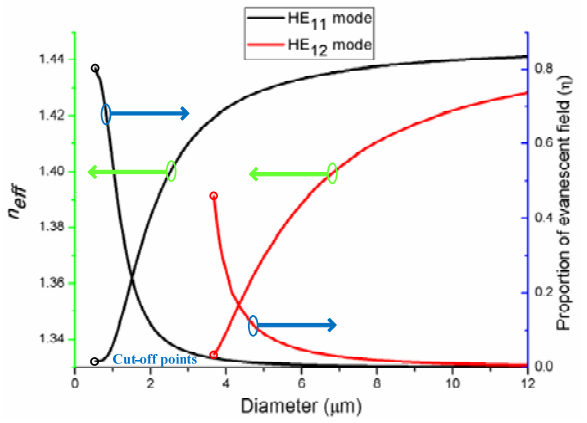

Fig. 2. Calculated effective RI (n_{eff}) and the proportion of evanescent field (η) of HE_{11} and HE_{12} modes with different diameters @ SRI =1.3320.

Actually, for SRI of 1.3320, when diameter is larger than 6.6μm, HE_{13} mode is also supported in theory. The Reference [23] experimentally proves that only HE_{1m} modes are supported in a microfiber. Meanwhile, when the diameter of MMMF is smaller than 12μm, the interference is mainly happened between the HE_{11} and HE_{12} modes, due that the HE_{13} mode can not be effectively excited. Consequently, the RI sensitivity of dip λ_m i.e. S can be calculated through the following equation by transforming Eq. (1) [25]:

$$\begin{aligned}S = \frac{d\lambda_m}{dn_{SRI}} &= \frac{\lambda_m \,\partial(\Delta n_{eff})/\partial n_{SRI}}{\Delta n_{eff} - \lambda_m \,\partial(\Delta n_{eff})/\partial \lambda_m} \\ &= \frac{\lambda_m}{G}\frac{\partial(\Delta n_{eff})}{\partial n_{SRI}}\end{aligned} \quad (3)$$

where $G = \Delta n_{eff} - \lambda_m \times \partial(\Delta n_{eff})/\partial \lambda_m$ is the group effective RI difference between HE_{11} mode and HE_{12} mode in MMMF. This equation directly shows that S is decided by λ_m, G, and $\partial(\Delta n_{eff})/\partial n_{SRI}$, but not affected by the fiber length. However, we assume that λ_m is around 1550nm, and the variation of λ_m is always around dozens of nanometers to be neglected. G and $\partial(\Delta n_{eff})/\partial n_{SRI}$ are dominated by the diameter of MMMF and n_{SRI}.

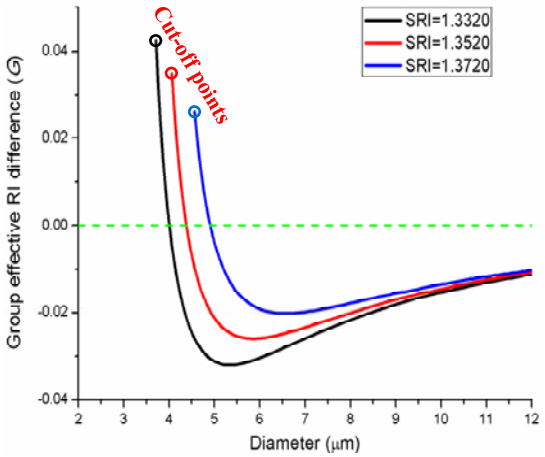

Fig. 3. Calculated group effective RI difference (G) along with MMMF diameter variation in SRI of 1.3320, 1.3520, and 1.3720.

Based on Eq. (1), we calculate the group effective RI difference (G) of the microfiber with different diameters and different surrounding RI.

From the numerical result shown in Fig. 3, it is clear that there are three regions i.e. G>0, G=0, and G<0. For G>0, G decrease rapidly from the cut-off point. For G<0, the absolute value of G firstly decrease and then increase towards to the same value, while the sigh of G is always negative. Moreover, for n_{SRI} =1.3320, 1.3520, and 1.3720, the variation trend of the sensitivity are similar, while the diameters corresponding to the turning point of G from positive to negative are gradually increased from 4.02μmto 4.94μm. Hence, we can infer that the turning point will shift to larger diameter when SRI increases.

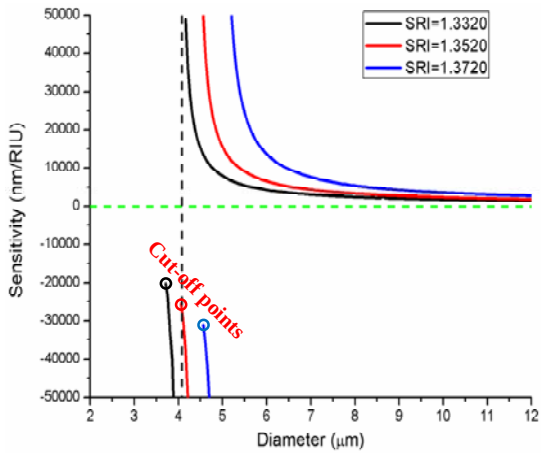

Fig. 4. Calculated RI sensitivity along with MMMF diameter variation at SRI of 1.3320, 1.3520, and 1.3720.

Fig. 4 shows the calculated RI sensitivities of MMMF with diameter ranging from 2μm to 12μm at different SRI. The turning point of the RI sensitivity appears at the same fiber diameter with that of G as $\partial(\Delta n_{eff}) / \partial n$ is always a negative value. When diameter is larger than the turning point, positive RI sensitivity is achieved; and on the other side of the turning point, negative RI sensitivity is obtained. It can be seen at the turning point, G approaches zero, and then the RI sensitivity is enhanced significantly to ±∞. In addition, on both sides of the turning point, the RI sensitivity varies rapidly and can easily reach to 10^4nm/RIU and above. For example, when n_{SRI} is 1.3520, the turning point of the fiber diameter is 4.40um，and the RI sensitivities are -49782nm/RIU and 49564nm/RIU at the diameter of 4.21μm and 4.56μm, respectively. So, for a certain SRI, the value and sign of the RI sensitivity can be flexibly tuned by controlling the diameter of the MMMF. It can be noticed that the turning point of RI sensitivity also exists in long period grating (LPG) [26] and highly birefringent microfiber (HBM) [25], while the MMMF exhibits the superiorities of relatively higher sensitivity, compact size and simple fabrication.

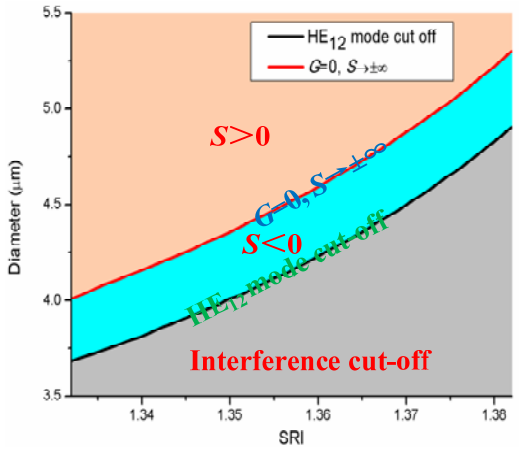

Fig. 5. Relationship between the SRI, the MMMF diameter, G, and S.

Furthermore, Fig. 5 demonstrates the relationship between the SRI, the MMMF diameter, G, and S. The line of G=0 and the line of HE_{12} mode cut-off divide the distribution of S into three regions i.e. S>0，S<0, and interference cut-off. The interference cut-off region corresponding to the occasion that only HE_{11} mode is supported while HE_{12} mode is cut-off. Along with the diameter increase, these three regions appear in sequence. The negative RI sensitivity only exists in a very narrow diameter range of about 0.3um, which is difficult to control in practical MMMF fabrication. However, we can optimize the diameter from upside and close to the line of G=0, and thus a much enhanced positive S will be obtained.

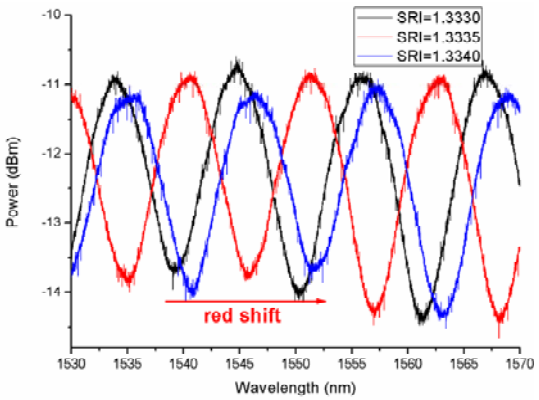

(a)

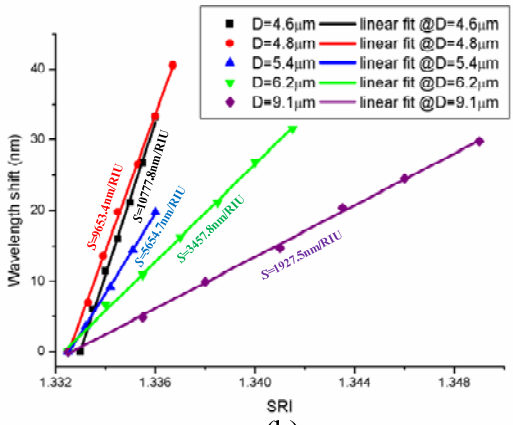

(b)

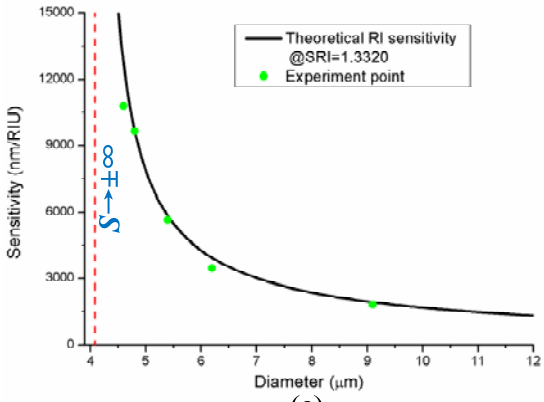

(c)

Fig. 6. (a) Typical transmission spectra of MMMF with diameter of 4.6μm at SRI around 1.3325. (b) Linear fit of wavelength shift to SRI with different fiber diameters of 4.6μm, 4.8μm, 5.4μm, 6.2μm, and 9.1μm. (c) The marked experimental sensitivities in the simulation curve.

In order to verify the validity of theoretical analysis, we measure the RI sensitivities of the MMMF with different diameters. Our experimental setup contains the sensing structure, an interrogation system (Micron Optics, Inc., sm125-500) including a broadband light source ranging from 1510nm to 1590nm, an optical spectrum analysis with wavelength scanning interval of 5 pm and resolution of 1pm, and a signal processing system used to analyze and demodulate the transmission spectrum. The RI sensing measurement is implemented by immersing the MMMF in different concentrations of glycerin solution.

Fig. 6(a) illustrates the typical transmission spectrums of MMMF with diameter of 4.6μm in SRI of 1.3330, 1.3335, and 1.3340. The experimental results reveal that the resonant dip shifts to longer wavelength when SRI increases. As we can see, the dip shifts about 5nm with SIR increases only 5×10^{-4}, and the RI resolution could reach to 1×10^{-7} with 1pm interrogation resolution.

Fig. 6(b) shows the linear fits of wavelength shifts along with the SRI variation for the MMMF with diameters of 4.6μm, 4.8μm, 5.4μm, 6.2μm, and 9.1μm, achieving the sensitivity of 10777.8nm/RIU, 9653.4nm/RIU, 5654.7nm/RIU, 3457.8nm/RIU, and 1927.5nm/RIU, respectively. For the measurement accuracy, we take the results with the maximum RI sensitivity of 10777.8nm/RIU as an example. The actual RI of the samples calibrated by the Abbe refractometer are 1.3330, 1.3335, 1.3340, 1.3345, 1.3350, 1.3355, 1.3360, respectively, while the calculated measurement values are 1.33296, 1.33352, 1.33402, 1.33445, 1.33493, 1.33544, and 1.33604, corresponding to the wavelength shifts of 0nm, 5.986nm, 11.433, 16.058, 21.169, 26.727, and 33.223, respectively. Therefore, the maximum deviation between the actual RI and measured RI is 7×10^{-5}, which is smaller than the accuracy of the Abbe refractometer. Admittedly, the direct measurement range is limited by the relatively narrow fringes of the interference spectrum. However, by using the real-time wavelength tracking method [27], the dynamic range can be greatly improved to the operating wavelength range of broadband light source (BBS), which far exceeds the width of free spectrum range (FSR).

Fig. 6(c) presents the comparison of the experimental sensitivities to the simulation results. In this figure, the green solid points represent the experimental sensitivities of MMMF with different diameters, and the black curve is the theoretical RI sensitivities at SRI of 1.3320. The theoretical RI sensitivities for MMMF with diameter of 9.1μm, 6.2μm, 5.4μm, 4.8μm, and 4.6μm in SRI of 1.3325 are 1949.7nm/RIU, 3974.2nm/RIU, 5901.8nm/RIU, 9841.2nm/RIU, and 12945nm/RIU, respectively. It is obvious that when the diameter approaches to 4μm, the sensitivity increase dramatically. Meanwhile, the experimental sensitivities and variation trend exhibit high consistency with the simulation results, which proves that the RI sensitivity beyond 10^5 nm/RIU as well as negative RI sensitivity can be realized by further decrease the MMMF diameter. The ultra-high RI sensitivity has great significance on trace detection in chemical and biological sensing applications. In practical applications, the MMMF could be enclosed in plastic or glass tube with the inject and outlet ports of solution to make the senor more robust and reliable [11].

In conclusion, we have comprehensively analysis the RI sensitivity properties of MMMF. To the authors' knowledge, the turning point of MMMF based in-line MZI sensor is firstly demonstrated, and both ultra-high positive and negative RI sensitivity can be obtained near the turning point. Moreover, high sensitivity of 10777.8nm/RIU at the fiber diameter of 4.6μm is achieved, and the experimental sensitivities and variation trend exhibit high consistency with the simulation result. The MMMF based in-line MZI sensors have great potential application in chemical and biological sensing fields due to the merits of high sensitivity, very simple and compact structure, low cost and easy fabrication.

National Natural Science Foundation of China (61275004); The sub-Project of the Major Program of the National Natural Science Foundation of China (61290315); The European Commission's Marie Curie International Incoming fellowship (328263); The Natural Science Foundation of Hubei Province for Distinguished Young Scholars (2014CFA036).

References

1. G. Huyang, J. Canning, M.L. Aslund, D. Stocks, T. Khoury, and M.J. Crossley, Opt. Lett. **35**, 817 (2010).
2. G. Coviello, V. Finazzi, J. Villatoro, and V. Pruneri, Opt. Express **17**, 21551 (2009).
3. G.T. Kanellos, G. Papaioannou, D. Tsiokos, C. Mitrogiannis, G. Nianios and N. Pleros, Opt. Express **18**, 179 (2010).
4. M. Bravo, A.M.R. Pinto, M. Lopez-Amo, J. Kobelke, and K. Schuster, Opt. Lett. **37**, 202 (2012).
5. C. Perrotton, R.J. Westerwaal, N. Javahiraly, M. Slaman, H. Schreuders, B. Dam, and P. Meyrueis, Opt. Express **21**, 382 (2013).
6. H.S Jang, K.N. Park, J.P. Kim, S.J. Sim, O.J. Kwon, Y.G. Han, and K.S. Lee, Optics Express, **17**, 3855 (2009).
7. S.M. Tripathi, W.J. Bock, P. Mikulic, R. Chinnappan, A. Ng, M. Tolba, and M. Zourob, Biosensors and Bioelectronics, **35**, 308 (2012).
8. B. Luo, Z. Yan, Z. Sun, J. Li, and L. Zhang, Optics Express, **22**, 30571 (2014).
9. L. Tong, R.R. Gattass, J.B. Ashcom, S. He, J. Lou, M. Shen, I. Maxwell, and E. Mazur, Nature **426**, 816 (2003).
10. G.S. Delgado, D.M. Hernandez, A.M. Rios, G.A.C. Sevilla, and J. Villatoro, Opt. Lett. **37**, 1974 (2012).
11. J.J. Zhang, Q.Z. Sun, R.B. Liang, J.H. Wo, D.M. Liu, and P. Shum, Opt. Lett. **37**, 2925 (2012).
12. B.M. Felipe, H.O. Jonas, R.B. Claudecir, and C.M.B. Cordeiro, J. Lightwave Technol. **31**, 2756 (2013).
13. F. Xu, P. Horak, and G. Brambilla, Opt. Express **15**, 7888 (2007).
14. M. Sumetsky, Opt. Express **12**, 2303 (2004).
15. W. Fan, J. Gan, Z. Zhang, X. Wei, S. Xu, and Z. Yang, Opt. Lett. **37**, 4323 (2012).
16. P. Wang, T. Lee, M. Ding, Z. Lian, X. Feng, Y. Ma, L. Bo, Q. Wu, Y. Semenova, W. Loh, G. Farrell, and G. Brambilla, J. Lightwave Technol. **32**, 40 (2014).
17. T. Wang, X. Li, F. Liu, W. Long, Z. Zhang, L. Tong, and Y. Su, Opt. Express **18**, 16156 (2010).
18. H. Luo, Q. Sun, Z. Xu, D. Liu, and L. Zhang, Opt. Lett. **39**, 4049 (2014).
19. L.L. Xu, Y. Li, and B.J. Li, Appl. Phys. Lett. **101**, 153510 (2012).
20. W.B. Ji, H.H. Liu, S.C. Tjin, K.K. Chow, and A. Lim, IEEE Photon. Technol. Lett. **24**, 1872 (2012).
21. H. Luo, Q. Sun, Z. Xu, W. Jia, D. Liu, and L. Zhang, IEEE Photon. Journal **7**, 7100908 (2015).
22. Y. Xue, Y.S. Yu, R. Yang, C. Wang, C. Chen, J.C. Guo, X. Zhang, C.C Zhu, and H.B. Sun, Opt. Lett. **38**, 1209 (2013).
23. A.J. Fielding, and C.C. Davis, J. Lightwave Technol. **17**, 1649 (1999).
24. L.M. Tong, J.Y. Lou, and E. Mazur, Opt. Express **12**, 1025 (2004).
25. J. Li, L.P. Sun, S. Gao, Z. Quan, Y.L. Chang, Y. Ran, L. Jin, and B.O. Guan, Opt. Lett. **36**, 3593 (2011).
26. X. Shu, and L. Zhang, J. Lightwave Technol. **20**, 255 (2002).
27. C. Gouveia, M. Zibaii, H. Latifi, M.J.B. Marques, J.M. Baptista, and P.A.S. Jorge, Sensor Actuat B-Chem **188**, 1212 (2013).